List of authors

Jiří Zahradník
Faculty of Mathematics and Physics, Charles University, Prague, Czech Republic
(jiri.zahradnik@matfyz.cuni.cz)

Fatih Fatih
Boğaziçi University, Kandilli Observatory and Earthquake Research Institute, Istanbul, Turkey (fthturhan@gmail.com)

Efthimios Sokos
Seismological Laboratory, Geology department, University of Patras, Greece
(esokos@upatras.gr)

František Gallovič
Faculty of Mathematics and Physics, Charles University, Prague, Czech Republic
(frantisek.gallovic@matfyz.cuni.cz)

Asperity-like (segmented) structure of the 6 February 2023 Turkish earthquakes

Jiří Zahradník[1], Fatih Turhan[2], Efthimios Sokos[3], František Gallovič[1]
[1]Faculty of Mathematics and Physics, Charles University, Prague, Czech Republic.
[2]Boğaziçi University, Kandilli Observatory and Earthquake Research Institute, Istanbul, Turkey.
[3]Seismological Laboratory, Geology department, University of Patras, Greece.

E-mail: jiri.zahradnik@matfyz.cuni.cz, fthturhan@gmail.com, esokos@upatras.gr, frantisek.gallovic@matfyz.cuni.cz.

Abstract
Key to studies of the rupture process is the identification of its major segmentation into asperities. Common multi-parametric methods invert for a continuous slip distribution; they usually rely on a predefined fault position, nucleation point, planarity, smoothing, etc. Here we propose more flexible low-parametric inversions - multi-point seismic source models, and multi-patch GPS models. We study the recent Mw 7.8 and 7.5 earthquakes in the Eastern-Anatolian fault system, recorded in a high-quality near-regional network of seismic strong motion and GPS stations. Using 40 seismic stations at epicentral distances ~20-300 km, we seek position, time, and DC-constrained mechanism of point-source subevents by a modified iterative deconvolution. We robustly resolve a small number of major asperities and demonstrate bilateral moment release for both earthquakes. Variations of the focal mechanism along the mapped faults are indicated. The inversion of GPS data for finite-fault patches confirms the asperity-like character of the events and validates along-fault changes of the focal mechanism.

Introduction

Large earthquakes are not only investigated as disastrous natural phenomena but also because they provide physical information about rupture propagation. Earthquake ruptures often evolve along several fault segments; this may be the case of events separated by years (Scotia Sea; Vallée and Satriano, 2014) days (Ridgecrest in California; Wang et al., 2020), minutes (Ahar–Varzaghan in Iran; Momeni et al., 2019), or seconds (Muji in China; Bie et al., 2018; L'Aquila in Italy; Cirella et al., 2012), to mention a few. The multiple segments are the key to examining geological and physical fault heterogeneities that affect the ruptures, radiated waves, and strong-motion damaging effects, and, in a longer perspective, are important for earthquake hazard assessment. Segments may have a different focal mechanism, e.g. strike-slip varying along curved faults. In mixed-type faulting events, the segments may even have different faulting styles, e.g., strike-slip and reverse (Kaikoura in New Zealand; Xu et al., 2018; Marmara Sea in Turkey; Turhan et al., 2023).

Seismic data, possibly combined with satellite geodesy data, are typically inverted for a continuous kinematic space-time slip distribution on a predefined plane or several planar segments. More advanced dynamic source models (Ulrich et al., 2019; Gallovič et al., 2020; Premus et al., 2022) use similar parametrizations, but these are beyond the scope of the present paper. The kinematic methods date back to Hartzell et al. (1989) and came through many improvements so that some of them (e.g. Ji et al., 2002) are already applied on a

routine level (https://earthquake.usgs.gov/data/finitefault/). As a rule, results for the same event differ between different researchers, dependent on the (multi-parametric) inverse problem formulation, physical parametrization, and numerical stabilization (Mai et al., 2016). Further spread in results can be caused by inappropriate station distribution or inaccurate velocity models. Thus, resolving stable features of the spatially and temporarily complex slip distributions, particularly the major asperities, is a challenge. One of the potentially best approaches to resolve common slip features from a variety of solutions consists in applying singular value decomposition and truncating to eigenvalues above a certain threshold (Gallovič and Ampuero, 2015).

The other approaches to reveal multi-segment ruptures are the methods formulated as low-parametric inverse problems, e.g. characterizing earthquakes as multi-point sources (MPS) whose position, time, moment, and focal mechanism are generally free. Pioneering work on MPS started with iterative deconvolution of teleseismic body waves, e.g. Kikuchi and Kanamori (1991). Delouis (2014) successfully represented a finite source by point sources for earthquakes of magnitudes from 4.5 to 9.0. Joint inversion for multi-point contributions in Bayesian formulations, based on W-phase, was applied to large earthquakes, e.g. by Duputel and Rivera (2017). Shimizu et al. (2020) proposed a method how to trace the variation of the centroid-point potency-rate-density tensors along faults. Recently methodic improvements of iterative deconvolution were proposed by Yue and Lay (2020). MPS inversions at regional distances have been less common. They started with the first release of Isola code (Zahradnik et al., 2005), where the acronym stands for “isolated asperities”. The name expresses the main idea: Since earthquakes typically contain a low number of asperities (patches, sub-sources, subevents), e.g. 2-3, not 10 or more, as empirically demonstrated by Somerville et al. (1999), it is useful to seek them directly rather than to infer potential earthquake segmentation from simplistic (over-smoothed) or wild (under-smoothed) slip inversions.

Since 2005, the Isola code has been continuously upgraded (Sokos and Zahradnik, 2013; Sokos et al., 2016; Zahradnik and Sokos, 2018) and increasingly applied to reveal earthquake complexities (Liu et al., 2018; Liu and Zahradnik, 2020; Hicks et al, 2020). Besides low-parametric character, another advantage is that MPS solutions are robust to errors in earthquake location. It is because subevents are space-time grid-searched in an almost arbitrary set of trial source positions and times around any approximate hypocenter position and origin time. The rupture process is not a priori constrained to start at the hypocenter. A disadvantage is that although the subevent moment is retrieved, we cannot estimate the slip unless independent information about the subevent size (length, area) is available. Even the low-parametric MPS inversions are vulnerable to various parameter trade-offs. Therefore, for example, Duputel and Rivera (2017) preferred to fix the spatial positions of the subevents, Analogously, other constraints were discussed by Yue and Lay (2020). Particularly dangerous might be tradeoffs between space-time moment variations and non-double-couple (non-DC) moment tensors. The latter typically accompanies multi-type faulting events whose correct (100% DC) subevent structure can only be revealed if seeking DC-constrained subevents (Sokos et al., 2020).

Two disastrous earthquakes occurred on 6 February 2023 in Turkey in the East Anatolian Fault Zone (EAFZ), at a contact between the Anatolian microplate and the Arabian plate (Duman and Emre, 2013). This site is near the southwestern termination of the EAFZ segment that ruptured during the Mw 6.8 2020 earthquake (e.g., Taymaz et al., 2021) for

which dynamic inversion of Gallovič et al. (2020) revealed a cascading activation of several segments, possibly expected also in the 2023 events. The human and material losses caused by the recent 2023 events were enormous. Finite-source models (USGS) revealed kinematic rupture development on several planar segments. Melgar et al. (2023) modeled slip on curved faults and estimated variable rupture speed. Rosakis et al. (2023) and Okuwaki et al. (2023) indicated supershear stages. The latter also detected a back-propagating rupture.

Our goal in this paper is to find out whether regional strong-motion seismic and GPS data suggest a multi-asperity character of these earthquakes. i.e., how much seismic moment release was concentrated in a few fault patches and temporal episodes. To this goal, we invert seismic data for MPS models and GPS data for multi-patch models, both with simple though non-standard techniques.

Seismic data and method

We study the largest events of the earthquake disaster in Turkey on February 6, 2023, Events 1 and 2, Mw 7.8 (USGS) and Mw 7.5 (USGS), following each other within 9 hours. Hypocenters according to the KOERI location (http://www.koeri.boun.edu.tr/sismo/2/en/) are as follows: Event 1: 01:17:32.00, 37.1757° N, 37.0850° E, depth 5.5. km. Event 2: 10:24:47.00, 38.0818° N, 37.1773° E, depth 5.0 km.

Each event is investigated using 21 strong-motion (accelerographic) stations. For Events 1 and 2 we use stations at epicentral distances of ~25-270 km, and ~37-214 km, respectively. Stations were selected based on azimuthal distribution and data quality. The data quality checks concerned two issues. Major low-frequency instrumental disturbances were detected by visually inspecting non-filtered integrated raw data, e.g. at station 3135 (N-component), 3802 (N-component), 0122 (all components); such records were removed from inversions. Further, at a few stations, timing problems were detected by checking location residuals and comparing real and synthetic waveforms. The records were corrected like this: 6303 by -17.6 s, 0213 by -4.6 s, 0209 by -64.4 s, 2704 by + 22.9 s, 4624 by +1.4 s. The negative/positive correction means that the station clock was advanced/delayed. Thus, before inversion, the start time of the record had to be formally increased/decreased. We also detected two stations that could not be fitted at all, and the reasons remain unknown (5805 and 8003).

We used the software ISOLA (Zahradník and Sokos, 2018), recently validated by Sokos et al. (2020) and Turhan et al. (2023). ISOLA uses code AXITRA (Cotton and Coutant, 1997) for Green's functions in a 1D medium. We calculate Green's functions up to Nyquist frequency of resampled waveforms (1024 points, time step of 0.3 s). The 1D velocity model of Acarel et al. (2019) is employed. ISOLA inverts complete seismograms for a multi-point source model. Here, the codes have been specifically adjusted for the needs of the large events (computer speedup, realistic distribution of trial source positions). Standard iterative deconvolution was modified as detailed below.

A problem of the standard iterative deconvolution is that it biases the solution by releasing an almost complete moment in the first retrieved subevent. To avoid this effect, we enforce the so-called "slow moment release". It is achieved in each iteration step by replacing the calculated moment value of the subevent with its fraction (e.g., ¼, and

correspondingly increasing the number of searched subevents 4 times). In this way, we prevent a very strong moment concentration in just a single point, thus increasing the chance to identify several asperities, if they exist in an earthquake. Subevents are searched in a grid of trial source points designed along mapped faults (Reitman et al., 2023). The temporal grid search starts a few seconds before the origin time and ends at 70 or 40 seconds after the origin time for Events 1 and 2, respectively. In general, Isola calculates focal mechanism optionally as full moment tensor (MT), deviatoric MT, and DC-constrained MT. To avoid false non-DC components, here we prefer the DC-constrained MTs of the subevents (DC > 90%). Some tests, in which we need to completely suppress the trade-off between the mechanism and space-time rupture evolution, are made also with a constant (predefined) DC mechanism (see Supplementary material, Fig. S1).

Epicenter serves just as the origin of Cartesian coordinates and does not physically affect the results, i.e., the rupture is *not* constrained to initiate at the hypocenter. The initial tests concerned trial sources uniformly covering a horizontal plane in a large area, ~200 km x 200 km; they provided the largest subevents near the epicenter, confirming that the inversion is not considerably biased by the used station distribution. In the preparatory tests, the trial sources were distributed along the faults and in several discrete depths. The depth resolution was poor; here we report stable results at a constant depth of 7.5 km. The elementary moment-rate function of subevents is a triangle of duration 20 or 10 s (for Events 1 and 2, respectively). These empirically found values significantly improve data fit compared to the often-used delta function.

Several frequency ranges of the inversion of the double-integrated acceleration records were tested. Finally, to avoid instrumental noise, we adopt the minimum inverted frequency of 0.01 Hz and choose the maximum inverted frequency of 0.5 Hz. In this range, the same 4^{th}-order causal Butterworth filter is applied to real and synthetic data. The value 0.5 Hz is rather formal because the triangle duration effectively acts as a low-pass filter, thus preferentially fitting mainly the lower frequencies and producing solutions analogous to those with 0.01-0.05 Hz (Fig. S2). Nevertheless, the use of the maximum frequency of 0.5 Hz was advantageous, because it more easily identified errors in absolute data timing. The fit between real and synthetic band-pass filtered displacement waveforms is quantified with variance reduction, VR (<=1); VR = 0.83 and 0.56 for the maximum frequency of 0.05 and 0.5 Hz, respectively (examples in Fig. S3 and S4). Multi-point sources are demonstrated as a set of circles (Fig. 1); their size is proportional to the moment and color indicates rupture time. Concentric circles show multiple point sources detected by deconvolution in the same trial point; the physical meaning is that the moments of the individual subevents at such points are to be summed. The spatial concentration of subevents defines seismic "patches" of the moment release (asperities). Temporal concentration is referred to as "episodes".

Seismic model

Varying trial source positions, frequency ranges, and station subsets produce slightly variable results. The model features stable across these variations are summarized in Fig. 1, Tab. 1, and as follows. **Event 1** ruptured two branches of EAFZ, hereafter referred to as the SW and NE branches, with the "kink" between them, near the epicenter. The largest moment release occurred on the EAFZ, spatially centered at ~50 km from the epicenter, and temporarily centered ~20 s after origin time (i.e., lasting 10-30 s, Fig. S2). The other

episodes occurred both in the SW and NE branches, almost simultaneously (centered ~45 s after origin), indicating bilateral rupture. The northeastern patch's position (~120 km away from the fault kink, i.e. ~70 km from the major patch), as well as its moment and focal mechanism, is more robustly determined than the southwestern patches. The focal mechanisms of the major stages are left-lateral strike slips, which however differ in their strike between the SW and NE branches by about 30° (see also the test of Fig. S1). These gross variations are in agreement with the geometry of mapped fault traces. Detailed variations of focal mechanisms of Event 1 along the fault are less robust, particularly in small subevents. That is why the mechanisms of all subevents are not presented here. We only show in Fig. 1 and Tab. 1 the stable mechanisms, typical for the four major episodes. Their total moment is 4.5e20 Nm. As the low-frequency limit is 0.01 Hz, our total moment and the moment magnitude (Mw 7.7) of Event 1 is probably underestimated.

Event 2 (Fig. 1, Tab. 1) shows the major moment release spread up to ~25 km west and ~25 km east of the epicenter, temporally centered at ~9 s after origin time (i.e., lasting 4-14 s). Other significant episodes of Event 2 occurred at ~50 km west of the epicenter, temporarily centered at ~12-16 s (Fig. S5). The total moment is 2.3e20 Nm (Mw 7.5). The focal mechanism of the westernmost moment release indicates a mixed-type faulting (oblique normal). It is further supported by the normal mechanism of a nearby aftershock Mw 4.8 of 7 February, included in Fig. 1, that we inverted with Isola (frequency range 0.04-0.09 Hz, VR 0.86). Which faulting type might have accompanied the dominant left-lateral strike-slip during Event 2 needs to be investigated. The mixed-type faulting could then explain a possible non-DC character of Event 2, preliminarily indicated in one of the USGS solutions (the DC percentage as low as 34%). Regarding the easternmost fault branch of Event 2, a relatively weak later rupture was indicated in our models yet not robustly resolved.

Table 1. Multi-point seismic model of Events 1 and 2 (ordered with decreasing moment)

Major patches of Event 1							
Lat (°)	**Lon (°)**	**Time (s)**	**Strike (°)**	**Dip (°)**	**Rake (°)**	**Moment (Nm)**	**Temporal order**
37.6013	37.3516	22.6	234	85	-9	2.2614E+20	2nd
37.9501	38.0793	43.3	69	80	-3	1.0209E+20	3rd
37.4803	37.0489	10.9	31	87	23	0.7763E+20	1st
37.1093	36.6521	45.1	17	67	16	0.5618E+20	4th

Major patches of Event 2							
Lat (°)	**Lon (°)**	**Time (s)**	**Strike (°)**	**Dip (°)**	**Rake (°)**	**Moment (Nm)**	**Temporal order**
38.0612	36.9823	8.6	269	72	-14	0.9655E+20	1st
38.0072	37.3178	9.2	277	73	9	0.6074E+20	2nd
38.0402	36.6447	15.8	250	48	-47	0.5453E+20	4th
38.0687	36.7574	12.2	354	64	173	0.3486E+20	3rd

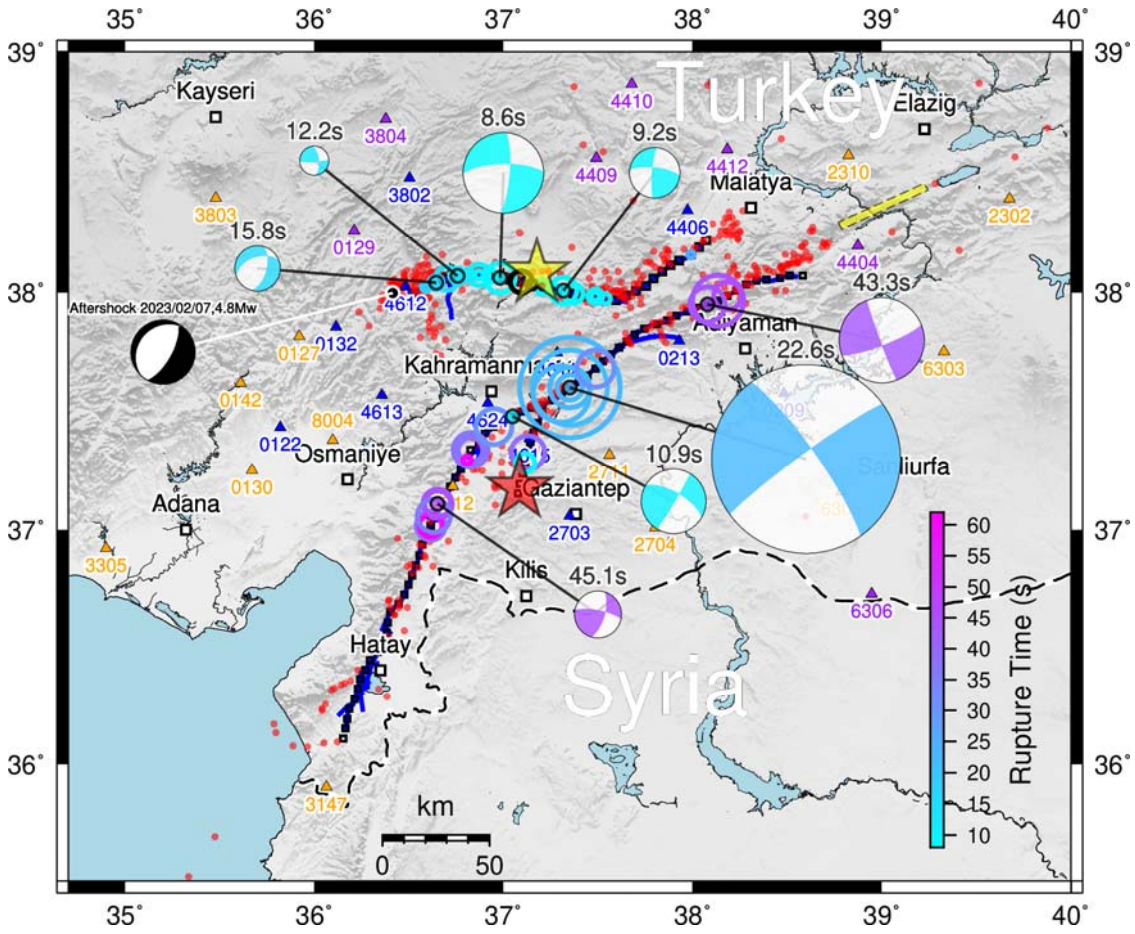

Fig. 1. *Multi-point seismic model (Tab. 1)*. Space-time moment release is shown by circles; the circles are sized according to moment and colored with centroid time relative to origin time (see the color scale). Focal mechanisms of the major rupture stages are plotted as equally colored beachballs (marked with time in seconds after origin). One normal-faulting aftershock is shown with a black beachball to demonstrate departures from dominant strike-slip faulting in the region. Epicenters are shown as stars (red – Event 1, yellow – Event 2). Used stations are plotted as triangles (orange – Event 1, blue – Event 2, and purple for both events). The grid of trial sources is shown with small black squares along the faults (blue lines) from Reitman et al. (2023). Aftershocks are shown as red dots according to AFAD (https://deprem.afad.gov.tr/event-catalog). The yellow rectangle depicts the rupture of the Elazığ 2020 Mw 6.8 earthquake from the dynamic inversion of Gallovič et al. (2020).

Improvement of the seismic model by GPS data

To validate and/or improve the seismic model we use published GPS static horizontal co-seismic displacements (Taymaz et al., 2023). Five stations with the largest offsets of at least > 10 cm in N or E components are used for Event 1, i.e. stations ANTE, ONIY, EKZ1, MLY1, and SIV1. In analogy with the seismic model, we perform a low-parametric inversion. Synthetic displacements are calculated according to Okada (1992). We invert the GPS data by jointly seeking moments at all trial source positions along the fault (the same points as previously used in seismic modeling). The inversion is made with the non-negative least squares method (Lawson and Hanson, 1974). At each point, the source is represented by an element with a uniform slip whose moment is to be determined. Each element is rectangular (horizontal and vertical size L and W, respectively, e.g. 20 km x 10 km, centered

at a depth of 7.5 km. The elements' length is greater than the separation of the trial positions (hence causing overlap) and serves as a stabilization of the inversion. Strike of the elements is randomly varied in a broad range from 10° to 80°; smaller variations are allowed for dip 80°-90° and rake from -20° to +20°. Thus the inversion also determines focal mechanisms. The random variations yield a suite of well-fitting solutions; their similarity indicates stable gross features of the moment distribution. The best-fitting solution, consistent with these stable features, is presented in Fig. 2 and Tab. 2. Total moment was fixed at 4.5e20 Nm (Mw 7.7). Similar results were obtained for L=10-40 km, moment constrained at 5e20 Nm or 6.0e20 Nm (Mw 7.8), or even for increased freedom in the varied mechanism.

Major robust results for Event 1 are as follows: (i) Most elements remain empty (= zero moments). The elements of non-zero moment release represent just a few (6) patches, A-F. The largest one, formed by two nearby (and overlapping) elements is situated 40 km NE of the epicenter. (ii) In spite of the freedom in the randomly varied element orientation, the best-fitting patches are mostly vertical and their strikes change in agreement with the fault curvature. (iii) Although the low number of patches and varying focal mechanisms were already captured by the seismic model, the stability of the focal mechanism in the GPS model is higher than in the seismic model. (iv) Comparing the GPS and seismic models can assign timing to the GPS patches: The GPS patches A+B (moment 1.74e20 Nm) are linked with 1st and 2nd seismic-model episode at 10-20 s (3.04e20 Nm), C+D (1.35e20 Nm) are linked with 3rd seismic episode at 43 s, NE of the epicenter (1.02e20 Nm), and E (0.52e20 Nm) is linked with 4th episode at 45 s, SW of the epicenter (0.56e20 Nm). Note of about 1e20 Nm moment deficiency in A+B. (v) The major feature missing in the seismic model is the GPS-inferred patch F (0.9e20 Nm) situated approximately 45 km south and 45 km west of the epicenter, row 3 of Tab. 2, which compensates for the moment deficiency of the GPS model. This patch was indicated in seismic inversions (Fig. S1, right panel), but was unstable regarding its position and mechanism, likely due to limited azimuthal coverage of the seismic stations toward the south.

Table 2. Multiple-patch GPS model of Event 1.

Lat (°)	Lon (°)	Strike (°)	Dip (°)	Rake (°)	Moment (Nm)	Patch*	Timing**
37.5490	37.2561	50	80	10	1.03E+20	B	2nd
37.9653	38.1346	60	90	0	0.89E+20	D	3rd
36.8057	36.5172	30	90	20	0.89E+20	F	? (Likely after 4th)
37.5009	37.0978	60	90	20	0.71E+20	A	1st
37.1092	36.6520	50	90	10	0.52E+20	E	4th
37.8487	37.7445	70	90	-10	0.46E+20	C	Likely before 3rd

* Denotation of the patch for Fig. 2 and Fig. 3

**The likely temporal order derived in analogy with the seismic model of Tab. 1

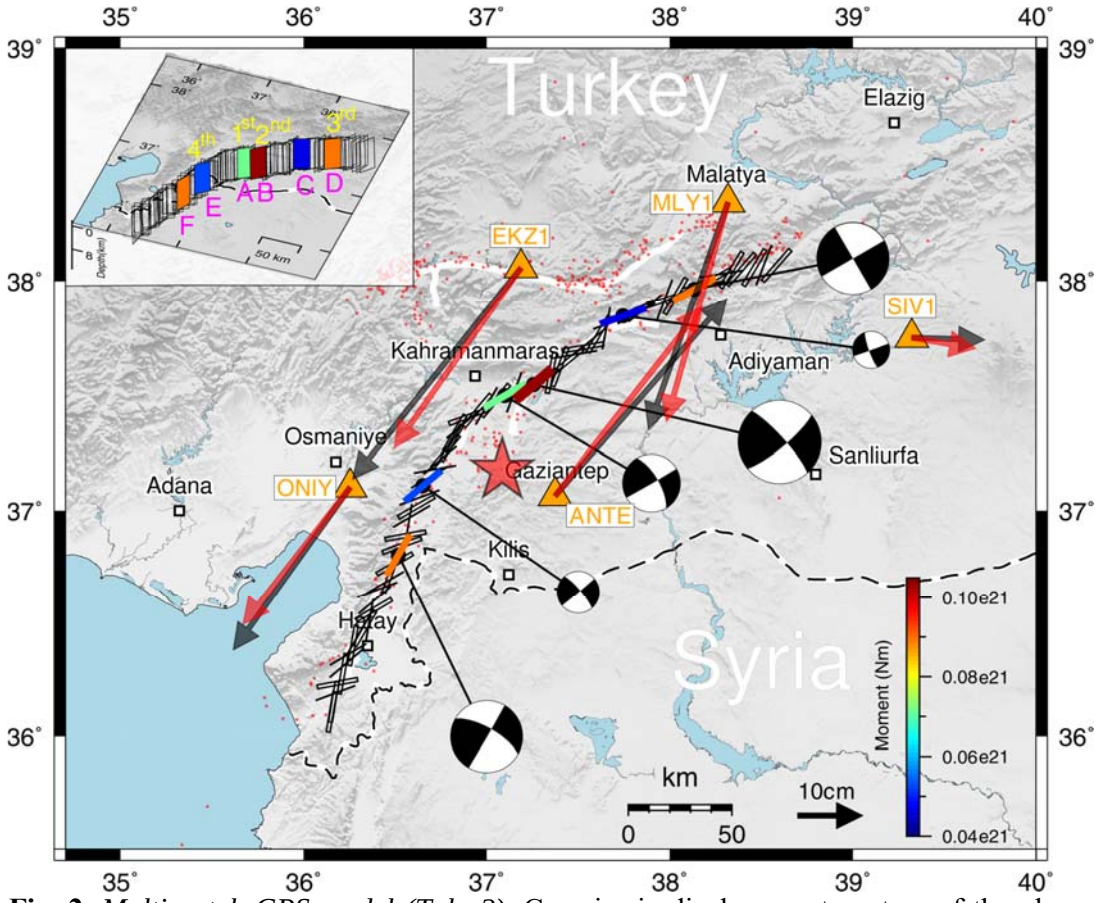

Fig. 2. *Multi-patch GPS model (Tab. 2).* Co-seismic displacement vectors of the observed (Taymaz et al., 2023) and modeled GPS data are shown by black and red arrows for the best-fit model. Six L=20 km x W=10 km non-zero elements of the best-fitting model are plotted as surface-projected rectangles colored relative to the moment. The inversion was made along the fault with randomized strike/dip/rake; one realization of the random geometry of the segments is shown. The empty rectangles have zero moments. Focal mechanisms resolved by GPS are shown by beachballs sized proportionally to the moment. As the almost vertical patches may not be well seen in the map view, the inset in the left-top corner provides an oblique view (azimuth 160°, elevation 40°, the depth scale is exaggerated by a factor of ~3.8). The denotation of the patches, A-F (Tab. 2) and 1^{st} – 4^{th} (Tab. 1) serves for comparison with Fig. 3 and Fig. 1.

Therefore, the seismic and GPS data indicate an uneven ("patchy", or asperity-like) structure of the rupture. To further validate this result, we also invert the GPS data of Event 1 for a continuous slip model (Fig. 3). We use LinSlipInv code (Gallovič et al., 2015), including smoothing by the covariance matrix of model parameters (k^{-2} dependence, where k is wavenumber). The results depend on the adopted relative smoothing weight (sw). The slip distribution and good data fit shown in Fig. 3 is for sw =2 (providing moment 4.8e20 Nm). The GPS data are almost equally well fitted for any sw < 2, producing even more concentrated patches than in the top panel. Moment decreases below 4.5e20 Nm both for sw < 0.8 and sw > 8.0. Thus the data fit and moment constraint determines a relatively narrow group of acceptable smoothing strengths, whose slip distribution is similar to Fig. 3. The result confirms a patch-like (segmented) moment release, as indicated in the previously discussed models of the present paper.

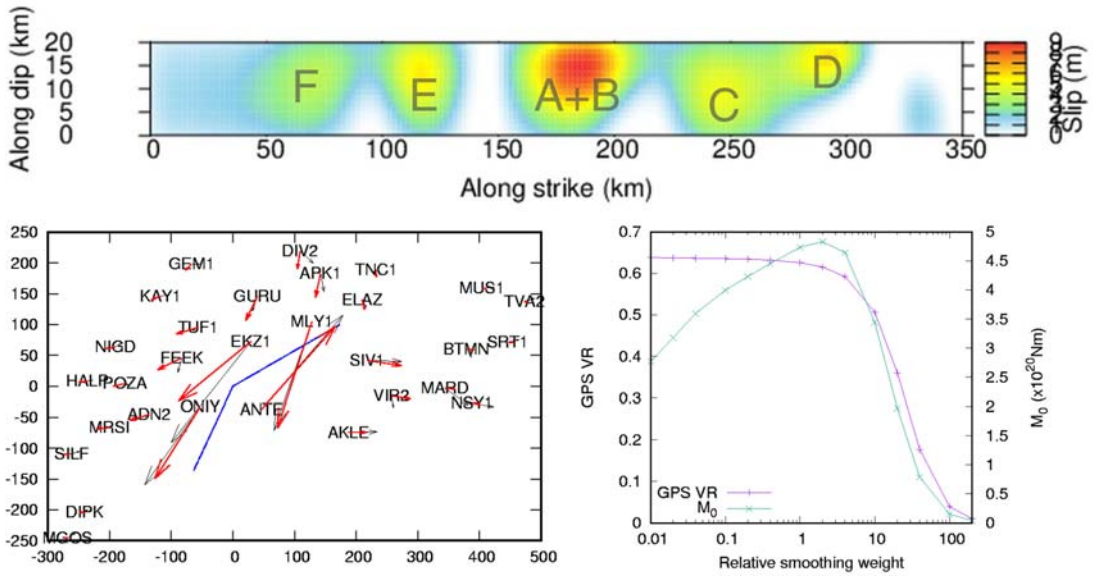

Fig. 3. *Continuous GPS model.* Top - the resulting slip distribution for relative smoothing weight sw = 2, corresponding to a good GPS data fit and the largest moment (4.8e20 Nm). Bottom left - the assumed fault (blue) consisting of two vertically dipping planar segments with rake=0. The kink of the fault is at the along-strike distance of ~150 km. Real and synthetic displacements are shown in black and red, respectively. Bottom right - the effect of smoothing upon GPS data fit (variance reduction, VR, magenta curve) and upon seismic moment Mo (cyan curve). Letters A to F show the similarity of the patches with Fig. 2.

Discussion and conclusion

The goal of the present paper was to find out whether regional strong-motion seismic and GPS data suggest a multi-asperity character of the 2023 Turkey earthquakes. The answer is positive. We performed multi-point source seismic modeling of Events 1 and 2 (Fig. 1 and Tab. 1), and multi-patch GPS modeling of Event 1 (Fig. 2 and Tab. 2). The modeling was facilitated by the availability of the mapped fault branches. Both modeling approaches consonantly show that moment release was spatially and temporarily concentrated. Emphasizing such an asperity-like concept we naturally do not fully exclude any possible small moment release in between the patches, contributing to the rupture transfer from one asperity to the other.

Joining results from the two inversions of **Event 1** we can define common features and link the GPS patches with the seismic timing: Patches A+B of the GPS model (moment 1.74e20 Nm), near the EAFZ kink, are linked with the 1st and 2nd seismic episodes (3.04e20 Nm), centered at 10-20 s after origin time. Considering the subevent triangular moment rate of duration 20 s, the A+B patches start near the origin time (0) and end near 30 s. Patches C+D (1.35e20 Nm) are linked with 3rd seismic episode (1.02e20 Nm) centered at 43 s, NE of the epicenter. Patch E (0.52e20 Nm) is linked with the 4th seismic episode at 45 s, SW of the epicenter (0.56e20 Nm). The reason for a moment deficiency in the GPS patches A+B compared to the 1st + 2nd seismic episode is unknown. Patch F (0.9e20 Nm), missing in the seismic model, was likely the last episode of Event 1 (likely temporarily centered at ~50 s) situated approximately 45 km south and 45 km west of the epicenter. Although this patch

was indicated in seismic inversions, it was not included in Tab. 1 because its position and mechanism were unstable. We speculate that this limited resolution was probably caused by limited azimuthal coverage of the seismic stations toward the south.

The seismic model of **Event 2** contains the initial major moment release within ~25 km west and ~25 km east of the epicenter, centered at ~9 s, i.e., approximately lasting up to ~14 s after origin time. This stage (the 1st and 2nd episode in Tab. 1) was followed mainly by the episode occurring ~50 km west of the epicenter (the 4th in Tab. 1), lasting up to ~21 s (Fig. S5), likely involving a normal-faulting component. The eastward development of Event 2 was seismically not well resolved, possibly because we did not follow an appropriate fault branch. Our inversion of the GPS data of the Nevada Geodetic Laboratory (Data and Resources) is less well posed than for Event 1 due to the strongly dominating 4.5-m displacement at a single station (the EKZ1 station, near the epicenter). Nevertheless, GPS inversion (Fig. S6) confirms the seismically inferred concept that Event 2 ruptured basically two main patches, around the epicenter, and near the western end of the considered fault.

If accepting the patch-like character of the earthquake, we should admit that each asperity might have operated with its own rupture style (bilateral, unilateral, different rupture speed), which is undeterminable by our modeling methods. That is why we cannot simply use the above estimates of the patch location and timing for estimating "mean rupture speeds". The detected and quantified segmentation of Events 1 and 2 will find application in high-frequency ground-motion simulations where asperities play a crucial physical role. Future studies should clarify the tectonic factors (fault steps, bends) that are behind the asperity-like faulting on the EAFZ. An open question of broader tectonic and physical significance is how and why Events 1 and 2 stopped their rupturing toward NE, close to the SW termination of the 2020 Elazığ Mw 6.8 rupture.

Acknowledgments
J.Z. and F.G. thank for the financial support from Czech Science Foundation, grant 23-06345S.

Data and Resources
Strong motion data used in this study were produced by the Disaster and Emergency Management Presidency of Turkey (AFAD - TK), https://tdvms.afad.gov.tr. We used GPS data of Event 1 from Taymaz et al. (2023), available at https://www.emsc-csem.org/Files/event/1218444/M7.8_updated_text_13-2-2023.pdf, provided by CORS-TR (TUSAGA-Aktif-Türkiye) administrated by General Directorate of Land Registry and Cadastre (TKGM) and General Directorate of Mapping (HGM). For Event 2, we used GPS data from the Nevada Geodetic Laboratory, http://geodesy.unr.edu/. We express our gratitude to all the staff involved in building and running high-quality Turkish networks. Code DC3D (Okada, 1992) is available at https://www.bosai.go.jp/e/dc3d.html. We used its modified version DC3Dmodif by F. Gallovič (unpublished). Continuous static GPS inversion was performed using LinSlipInv (http://fgallovic.github.io/LinSlipInv/). The patch-like GPS inversion was made with a yet unpublished code of J. Zahradník. The ISOLA software used in this paper (Zahradník and Sokos, 2018) can be downloaded from https://geo.mff.cuni.cz/~jz/for_ISOLAnews/ and https://github.com/esokos/isola. The maps were generated using the Generic Mapping Tools v6 (Wessel et al.,2019).

References

Acarel, D., M. D. Cambaz, F. Turhan, A. K. Mutlu, and R. Polat (2019). Seismotectonics of Malatya Fault, Eastern Turkey. Open Geosciences 11, 1098–1111, https://doi.org/10.1515/geo-2019-0085.

Bie, L., S. Hicks, T. Garth, P. Gonzalez, and A. Rietbrock (2018). 'Two go together': Near-simultaneous moment release of two asperities during the 2016 Mw 6.6 Muji, China earthquake, Earth and Planetary Science Letters, 491, 34-42, https://doi.org/10.1016/j.epsl.2018.03.033.

Cirella, A., A. Piatanesi, E. Tinti, M. Chini, M. Cocco (2012). Complexity of the rupture process during the 2009 L'Aquila, Italy, earthquake, Geophysical Journal International 190, 607–621, https://doi.org/10.1111/j.1365-246X.2012.05505.x.

Cotton F., and O. Coutant (1997). Dynamic stress variations due to shear faults in a plane-layered medium, Geophys. J.Int., 128, 676-688, doi: 10.5281/zenodo.4603722.

Disaster and Emergency Management Authority. (1973). Turkish National Strong Motion Network [Data set]. Department of Earthquake, Disaster and Emergency Management Authority. https://doi.org/10.7914/SN/TK

Duman, T. Y., and Öm Emre (2013). The East Anatolian Fault: geometry, segmentation and jog characteristics, Geol. Soc. Spec. Publ. 372, 495–529.

Duputel, Z., and L. Rivera (2017). Long-period analysis of the 2016 Kaikoura earthquake, Physics of the Earth and Planetary Interiors 265, 62–66. https://doi.org/10.1016/j.pepi.2017.02.004.

Gallovič, F., and J.-P. Ampuero (2015). A new strategy to compare inverted rupture models exploiting the eigenstructure of the inverse problem, Seismological Research Letters 86 (6), 1679–1689, doi: https://doi.org/10.1785/0220150096.

Gallovič, F., W. Imperatori, and P. M. Mai (2015). Effects of three-dimensional crustal structure and smoothing constraint on earthquake slip inversions: case study of the Mw6.3 2009 L'Aquila earthquake, J. Geophys. Res. 120, 428-449, doi:10.1002/2014JB011650.

Gallovič, F., J. Zahradník, V. Plicka, E. Sokos, Ch. Evangelidis, I. Fountoulakis, I., and F. Turhan (2020). Complex rupture dynamics on an immature fault during the 2020 Mw 6.8 Elazığ earthquake, Turkey. Commun. Earth Environ. 1, 40. https://doi.org/10.1038/s43247-020-00038-x.

Hartzell, S. (1989). Comparison of seismic waveform inversion results for the rupture history of a finite fault: application to the 1986 North Palm Springs, California, earthquake, J. Geophys. Res. 94, 7515–7534.

Hicks, S. P., R. Okuwaki, A. Steinberg, C. A. Rychert, N. Harmon, R. E. Abercrombie et al. (2020). Back-propagating supershear rupture in the 2016 Mw 7.1 Romanche transform fault earthquake, Nat. Geosci. 13(9), 568 647–653, doi:10.1038/s41561-020-0619-9.

Ji, C., D. J. Wald, and D. V. Helmberger (2002). Source description of the 1999 Hector Mine, California, earthquake, part I: Wavelet domain inversion theory and resolution analysis, Bull. Seismol. Soc. Am. 92, 1192–1207.

Kikuchi, M., and H. Kanamori (1991). Inversion of complex body waves—III, Bull. Seismol. Soc. Am. 81, 2335–2350.

Lawson, C.L., and R. J. (1974). Solving least squares problems. In: Prentice-Hall Series in Automatic Computation.

Liu, J., L. Li, J. Zahradník, E. Sokos, C. Liu, and X. Tian (2018). North Korea's 2017 test and its nontectonic aftershock, Geophys. Res. Lett. 45, doi: 10.1002/2018GL077095.

Liu, J., and J. Zahradník (2020). The 2019 MW 5.7 Changning earthquake, Sichuan Basin, China: A shallow doublet with different faulting styles. Geophys. Res. Lett. 47, e2019GL085408. https://doi.org/10.1029/2019GL085408.

Mai, P. M., Schorlemmer, D., Page, M., Ampuero, J.-P., Asano, K., Causse, M., Custódio, S., Fan, W., Festa, G., Galis, M., Gallovič, F., Imperatori, W., Käser, M., Malytskyy, D., Okuwaki, R., Pollitz, F., Passone, L., Razafindrakoto, H., Sekiguchi, H., Song, S.-G., Somala, S., Thingbaijam, K., Twardzik, C., van Driel, M., Vyas, J., Wang, R., Yagi, Y., Zielke, O. (2016). The Earthquake-Source Inversion Validation (SIV) Project, Seism. Res. Lett. 87, 690-708.

Melgar, D., T. Taymaz, A. Ganas, et al. (2023). Sub- and super-shear ruptures during the 2023 Mw 7.8 and Mw 7.6 earthquake doublet in SE Türkiye, pre-print, EarthArXiv, https://doi.org/10.31223/X52W9D.

Momeni, S., A. Aoudia, S. Tatar, C. Twardzik, and R. Madariaga (2019). Kinematics of the 2012 Ahar–Varzaghan complex earthquake doublet (Mw6.5 and Mw6.3). Geophysical Journal International 217 (3), 2097-2124, https://doi.org/10.1093/gji/ggz100.

Okada, Y. (1992). Internal deformation due to shear and tensile faults in a half-space. Bull. Seismol. Soc. Am. 82-2, 1018–1040.

Okuwaki, R., Y. Yagi, T. Taymaz, and S. P. Hicks (2023). Multi-scale rupture growth with alternating directions in a complex fault network during the 2023 south-eastern Türkiye and Syria earthquake doublet, pre-print, EarthArXiv, https://doi.org/10.31223/X5RD4W.

Premus, J., F. Gallovič, and J.-P. Ampuero (2022). Bridging time scales of faulting: From coseismic to postseismic slip of the Mw 6.0 2014 South Napa, California earthquake, Sci. Adv. 8, eabq2536, doi: 10.1126/sciadv.abq2536.

Reitman, Nadine G, Richard W. Briggs, William D. Barnhart, Jessica A. Thompson Jobe, Christopher B. DuRoss, Alexandra E. Hatem, Ryan D. Gold, and John D. Mejstrik (2023). Preliminary fault rupture mapping of the 2023 M7.8 and M7.5 Türkiye Earthquakes, https://doi.org/10.5066/P985I7U2.

Rosakis, A. J., M. Abdelmeguid, and A. Elbanna (2023). Evidence of early supershear transition in the Feb 6th 2023 Mw 7.8 Kahramanmaraş Turkey earthquake from near-field records, pre-print, EarthArXiv, https://doi.org/10.31223/X5W95G.

Shimizu, K., Y. Yagi, R. Okuwaki, and Y. Fukahata (2020). Development of an inversion method to extract information on fault geometry from teleseismic data, Geophysical Journal International *220*(2), 1055–1065, https://doi.org/10.1093/gji/ggz496.

Sokos, E., and J. Zahradník (2013). Evaluating centroid-moment-tensor uncertainty in the new version of ISOLA software, Seismol. Res. Lett. 84, 656–665, doi: 10.1785/0220130002.

Sokos, E., J. Zahradník, F. Gallovič, A. Serpetsidaki, V. Plicka, A. Kiratzi (2016). Asperity break after 12 years: The Mw6.4 2015 Lefkada (Greece) earthquake, Geophys. Res. Lett. 43, 6137–6145, doi:10.1002/2016GL069427.

Sokos, E., F. Gallovič, C.P. Evangelidis, A. Serpetsidaki, V. Plicka, J. Kostelecký, and J. Zahradník (2020). The 2018 M_W 6.8 Zakynthos, Greece, earthquake: Dominant strike-slip faulting near subducting slab. Seismol. Res. Lett., 1–12, https://doi.org/10.1785/0220190169.

Somerville, P., K. Irikura, R. Graves, S. Sawada, D. Wald, N. Abrahamson, Y. Iwasaki, T. Kagawa, N. Smith, and A. Kowada (1999). Characterizing crustal earthquake slip models for the prediction of strong ground motion, Seism. Res. Lett. 70, 59–80.

Taymaz, T., A. Ganas, S. Yolsal-Çevikbilen, F. Vera, T. Eken, C. Erman, D. Keleş, V. Kapetanidis, S. Valkaniotis, I. Karasante, V. Tsironi, P. Gaebler, D. Melgar, and T. Ocalan (2021). Source mechanism and rupture process of the 24 January 2020 Mw 6.7

Doğanyol-Sivrice earthquake obtained from seismological waveform analysis and space geodetic observations on the East Anatolian Fault Zone (Turkey), Tectonophysics 804, TECTO14240-228745, https://doi.org/10.1016/j.tecto.2021.228745.

Taymaz, T., A. Ganas, D. Melgar, B. W. Crowell, T. Öcalan (2023). no title (data), https://www.emsc-csem.org/Files/event/1218444/M7.8_updated_text_13-2-2023.pdf.

Turhan, F., D. Acarel, V. Plicka, M. Bohnhoff, R. Polat, and J. Zahradník (2023). Coseismic faulting complexity of the 2019 Mw 5.7 Silivri earthquake in the Central Marmara Seismic Gap, offshore Istanbul. Seismol. Res. Lett., 94 (1): 75–86. https://doi.org/10.1785/0220220111.

Ulrich, T., A. A. Gabriel, J. P. Ampuero, et al. (2019). Dynamic viability of the 2016 Mw 7.8 Kaikōura earthquake cascade on weak crustal faults. Nat Commun **10**, 1213, https://doi.org/10.1038/s41467-019-09125-w

Vallée, M., and C. Satriano (2014). Ten year recurrence time between two major earthquakes affecting the same fault segment, Geophysical Research Letters *41*(7), 2312-2318.

Wang, K., D. S. Dreger, E. Tinti, R. Bürgmann, and T. Taira (2020). Rupture process of the 2019 Ridgecrest, California Mw 6.4 foreshock and Mw 7.1 earthquake constrained by seismic and geodetic Data. Bulletin of the Seismological Society of America 110 (4): 1603–1626, https://doi.org/10.1785/0120200108.

Wessel, P., Luis, J. F., Uieda, L., Scharroo, R., Wobbe, F., Smith, W. H. F., and Tian, D. (2019). The Generic Mapping Tools version 6. Geochemistry, Geophysics, Geosystems, 20, 5556–5564. https://doi.org/10.1029/2019GC008515

Xu, W., G. Feng, L. Meng, A. Zhang, J. P. Ampuero, R. Bürgmann, and L. Fang. (2018). Transpressional rupture cascade of the 2016 Mw 7.8 Kaikoura earthquake, New Zealand. Journal of Geophysical Research: Solid Earth, 123, 2396–2409. https://doi.org/10.1002/2017JB015168

Yue, H., and T. Lay (2020). Resolving complicated faulting process using Multi-Point-Source representation: Iterative inversion algorithm improvement and application to recent complex earthquakes, Journal of Geophysical Research: Solid Earth 125, e2019JB018601, https://doi.org/10.1029/2019JB018601.

Zahradník, J., A. Serpetsidaki, E. Sokos, G.-A. Tselentis (2005). Iterative deconvolution of regional waveforms and a double-event interpretation of the 2003 Lefkada Earthquake, Greece, Bull. Seismol. Soc. Am. 95, 159–172, doi:10.1785/0120040035.

Zahradník, J., and E. Sokos (2018). ISOLA code for multiple-point source modeling—Review, in Moment Tensor Solutions: A Useful Tool for Seismotectonics, S. D'Amico (Editor), Springer International Publishing, Cham, Switzerland, 1–28, doi: 10.1007/978-3-319-77359-9_1. Also at https://geo.mff.cuni.cz/~jz/papers/ISOLA_bookchapter.pdf.

Supplementary material

Here we present particular tests explained in the figure captions.

Technical remark:
Formally, to define the origin of Cartesian coordinates, we used preliminary locations:
Event 1: Lat 37.218 , Lon 37.007; Event 2: Lat 38.0804, Lon 37.2235.
These positions are shown by stars in all figures of this supplement.

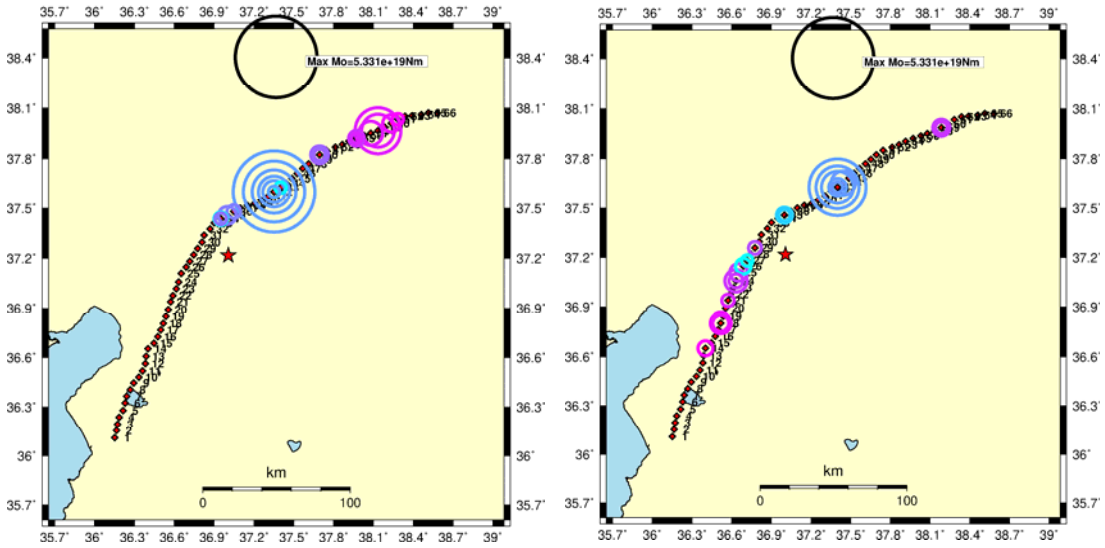

Fig. S1. Comparing space-time moment release for a constant, predefined strike-slip mechanism, strike/dip/rake(°) of 60/80/-5 typical for the NE fault segment (left), and another predefined strike-slip mechanism of 30/80/-5 typical for the SW fault segment (right). Note that the "NE" mechanism does not support any moment release on the SW segment. Similarly, the "SW" mechanism is not suitable for the NE segment except for the major slip. That major slip (in the right panel) is so robust that it persists near the epicenter even with the inappropriate ("SW") mechanism; however, such a slip patch is smaller and provides a worse waveform fit than with the correct ("NE") mechanism. This test demonstrates that both fault branches participated in the faulting, having unequal focal mechanisms, roughly consistent with the mapped faults. The colors vary from cyan to magenta as centroid time increases from 10 to 60 s after origin time. The scale for subevents' moment is shown by a black circle at the top.

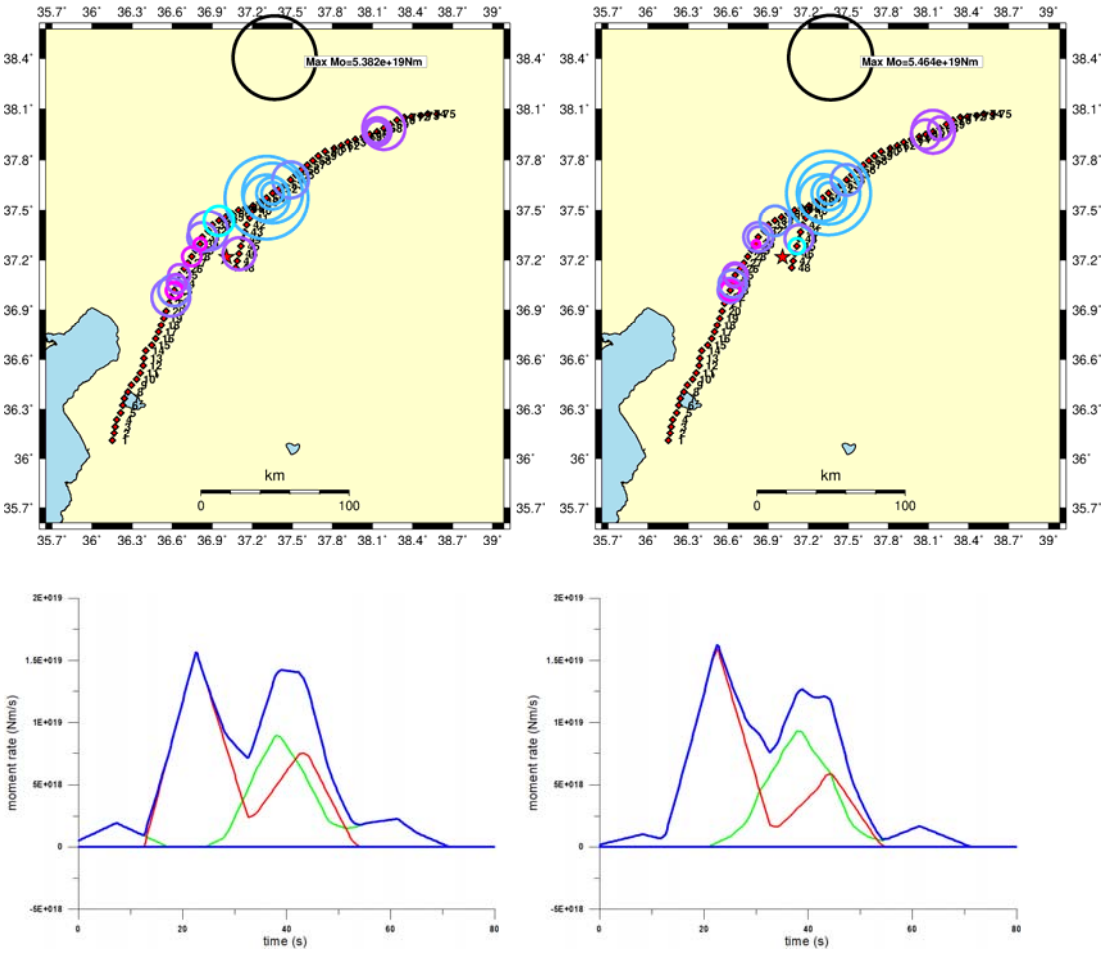

Fig. S2. Comparing space-time moment inverted in frequency ranges 0.01-0.05 (left) and 0.01-0.50 Hz (right). Basic features are the same because the 20-s triangular moment rate of the subevents acts as a low-pass filter. The colors vary from cyan to magenta as centroid time increases from 10 to 60 s after origin time. The cyan-color circles are scarce, the initial stage is poorly resolved. Bottom inset - the moment-rate functions assuming the subevents characterized by 20-s triangles. Red and green curves correspond to the NE and SW fault branches, respectively, and blue is the sum.

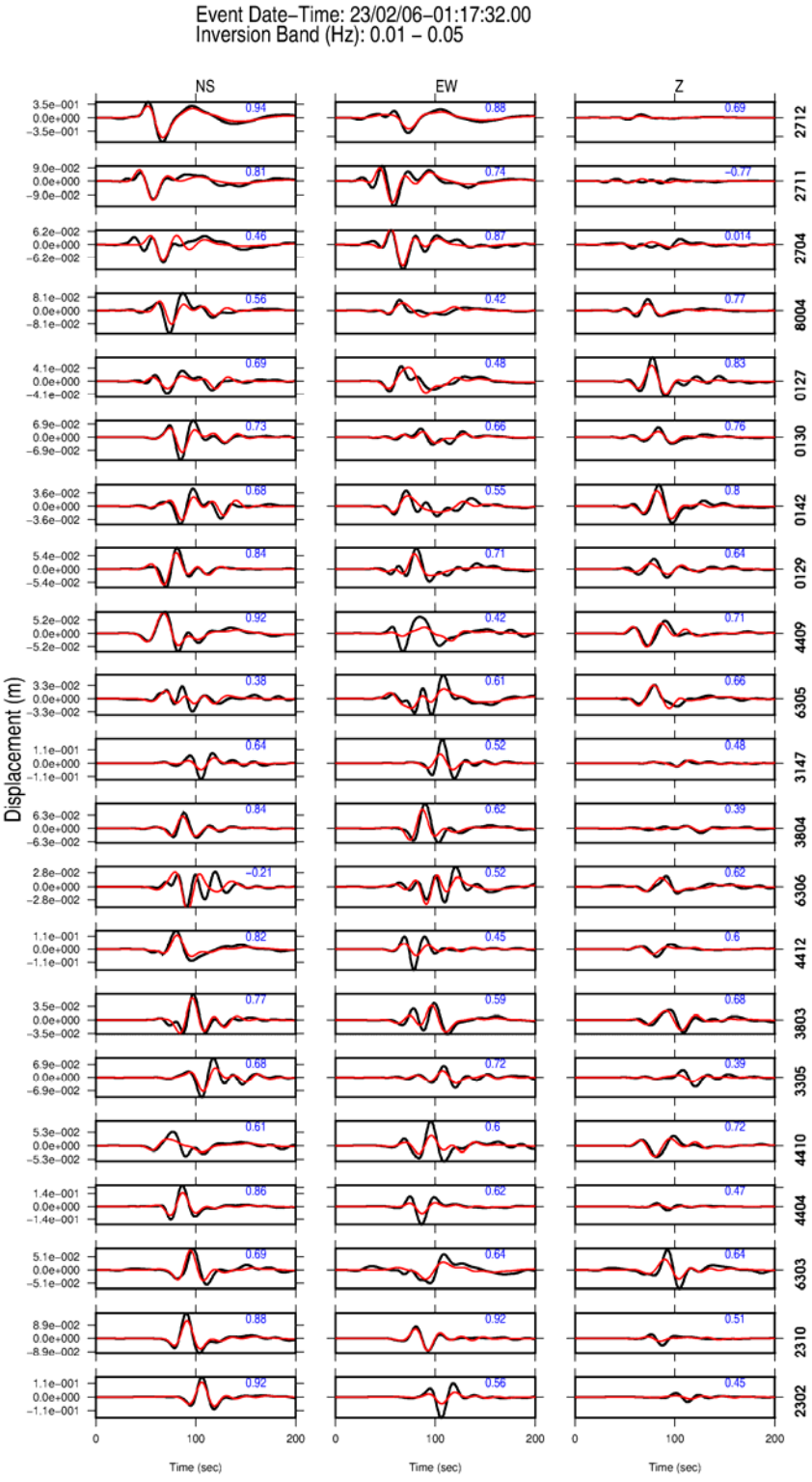

Fig. S3. Waveform fit for the model of Fig. S2 in the frequency range 0.01-0.05 Hz, VR 0.83. Blue numbers depict variance reduction per component.

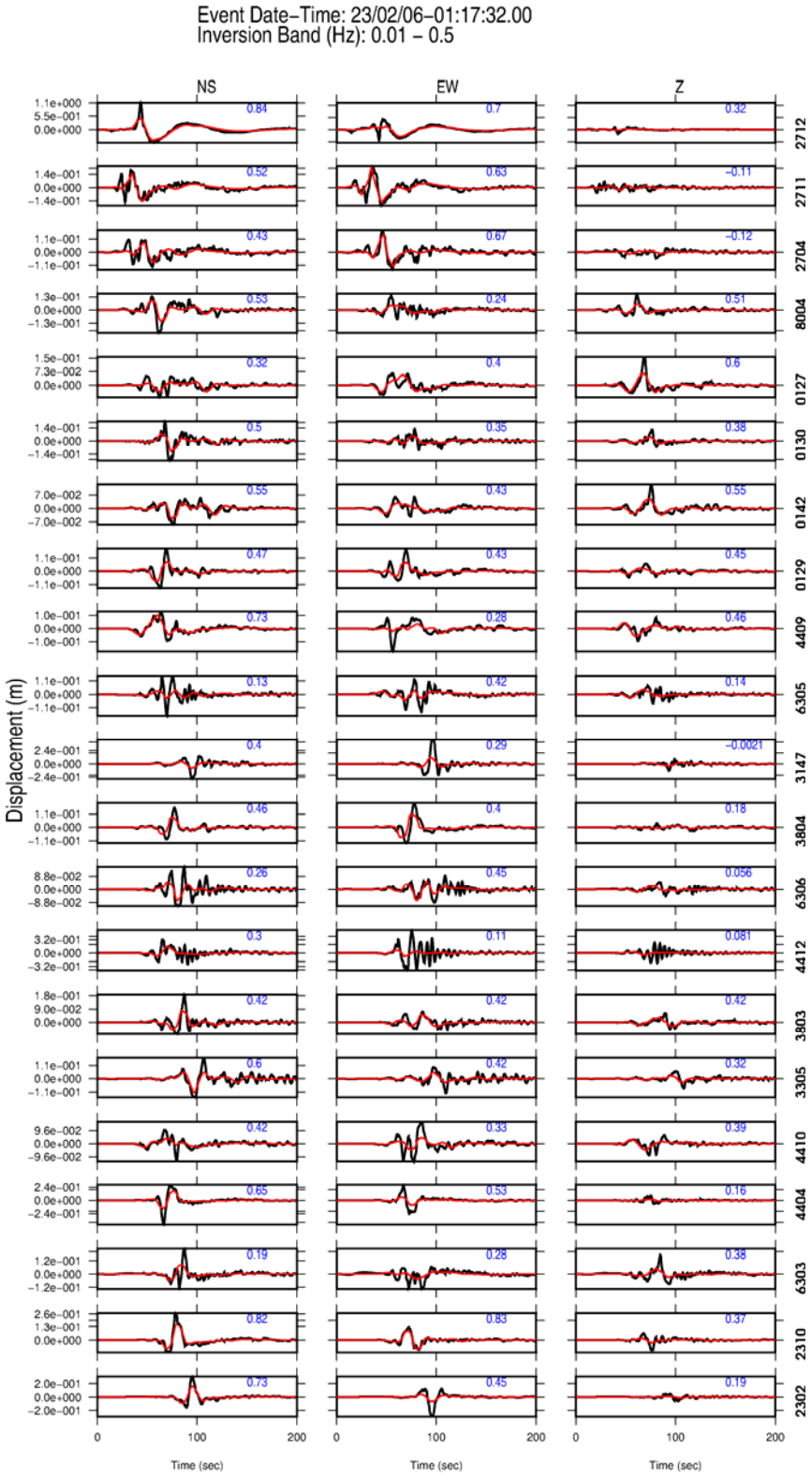

Fig. S4. Waveform fit for the model of Fig. S2 in the frequency range 0.01-0.50 Hz, VR 0.56. Blue numbers depict variance reduction per component.

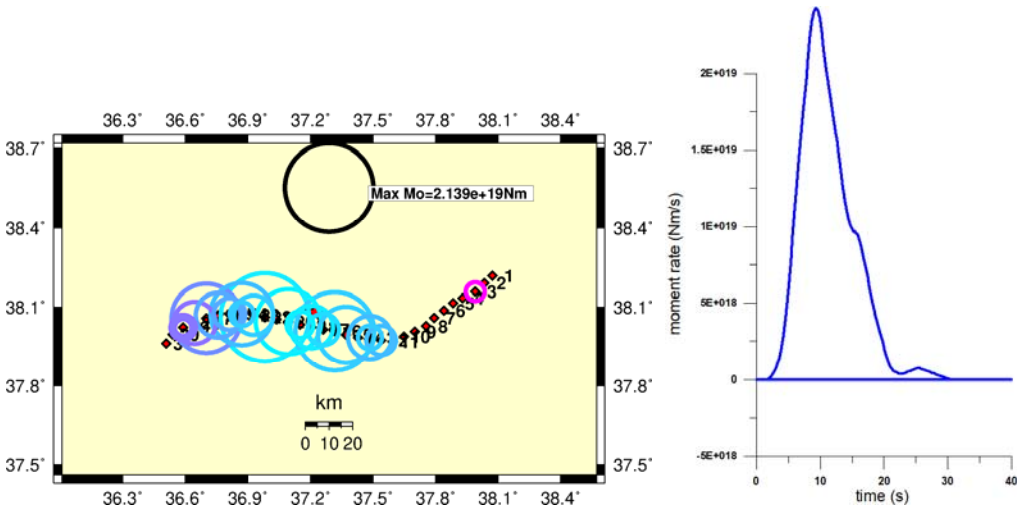

Fig. S5. Space-time moment release of Event 2. Close-up of the fault from Fig. 1 of the main text. Inversion in the frequency range 0.01-0.5 Hz, VR 0.64. The color scale for timing from cyan to magenta corresponds to time 6-25 s after origin time. The latest (poorly constrained) single subevent on the eastern SW-NE trending fault branch is at time 25 s. The majority of subevents on the W-E trending fault branch occurred at time 8-17 s. The scale for subevents' moment is shown by a black circle at the top. Right inset - the moment-rate function assuming the subevents characterized by 10-s triangles.

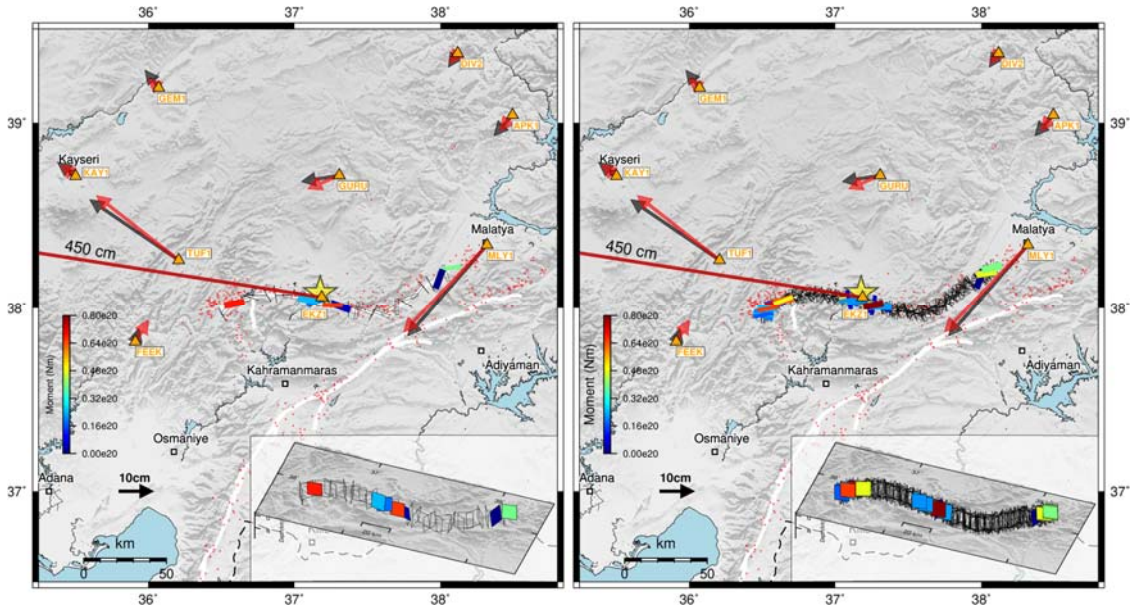

Fig. S6. GPS finite-patch inversion of Event 2. Denotation as in Fig. 2 of the main text. The arrows corresponding to EKZ1 station data (450 cm) are truncated at the left edge of the plot; however, their fit is perfect. Multiple empty rectangles show the allowed geometrical variation of the inverted elements along the fault. The elements (L = 10 km, W = 9 km) are centered at depth of 5 km. The elements colored with moment demonstrate the main patches, dominant near the epicenter (star) and in the western fault end. Left – the best-fit solution. Right – a suite of the almost equally well-fitting solution (uncertainty, to check the stability of the best-fit solution).